

## Electron holography and micromagnetic simulations unveil the magnetic domain structure of steel-embedded Fe<sub>3</sub>C carbides

Sami Kaappa<sup>a</sup>, Mads Søndergaard Larsen<sup>b</sup>, Suvi Santa-aho<sup>c</sup>, Murat Nulati Yesibolati<sup>b</sup>,  
 Mari Honkanen<sup>e</sup>, Kristian Speranza Mølhave<sup>b</sup>, Minnamari Vippola<sup>c,e</sup>, Lasse Laurson<sup>a</sup>,  
 Marco Beleggia<sup>b,d</sup>

<sup>a</sup> Computational Physics Laboratory, Tampere University, Korkeakoulunkatu 5, 33014 Tampere, Finland

<sup>b</sup> DTU Nanolab, Technical University of Denmark, Fysikvej 307, 2800 Kongens Lyngby, Denmark

<sup>c</sup> Engineering Materials Science, Tampere University, Korkeakoulunkatu 6, 33720 Tampere, Finland

<sup>d</sup> Department of Physics, University of Modena and Reggio Emilia, Via Campi 213/A, 41125 Modena, Italy

<sup>e</sup> Tampere Microscopy Center, Tampere University, Korkeakoulunkatu 3, 33720 Tampere, Finland

### ARTICLE INFO

#### Keywords:

Carbides

Magnetism

Electron holography

Lorentz microscopy

Transmission electron microscopy

Micromagnetic simulations

### ABSTRACT

The rapid development of spintronic devices brings about the need for more efficient experimental methods to explore magnetic domain structures and their response to external fields at the nano- to micrometer scale. Here, transmission electron microscopy (TEM) with inline and off-axis electron holography is used to investigate with nanometer resolution the magnetic domain and domain wall structures in cementite (Fe<sub>3</sub>C) carbides embedded in thin ferromagnetic steel films. The capabilities of the streamlined inline holography method are compared to those of the more resource-demanding off-axis electron holography. Micromagnetic simulations are employed to interpret the data analysis. The simulations are used specifically to resolve the internal domain wall structure along the film thickness/electron beam direction, which is inaccessible to non-tomographic TEM imaging methods. The cementite carbides reveal a peculiar striped magnetic structure with controllable and reversible properties under an applied external magnetic field.

### 1. Introduction

Domain wall (DW) dynamics in ferromagnetic materials underpins the functionality of magnetic devices in many applications, such as magnetic memories, logic devices, and spintronics [1–8], where especially the so-called racetrack memories have gained attention in the last few years [9–11]. Another field of applications for DW dynamics is the non-destructive testing (NDT) method based on magnetic Barkhausen noise (MBN), commonly utilized in industry for, e.g., quality control of ground surfaces [12,13]. The Barkhausen noise signal from the current in a small pick-up coil mounted on a material during magnetization originates from the interactions of moving domain walls with material defects. These hinder the smooth motion of DWs, producing a seemingly discontinuous increase in magnetization when a time-varying external magnetic field is applied. The tiny jumps in magnetization are read out as noise over the hysteresis curve by the pick-up coil. Using nanowires in racetrack memories also requires naturally formed or artificially produced defects to control magnetization [9,14] that need to be experimentally characterized. Thus, the development of applications based on both Barkhausen noise and spintronics benefits

from the detailed microscopic knowledge electron holography provides of domain walls structure and of their response to the applied magnetic fields or spin-polarized currents evaluated in different end-user cases.

Magnetic domains and domain walls can be imaged by several methods, depending on the required scale and resolution. For example: magneto-optic Kerr effect (MOKE) microscopy [15–17], magnetic force microscopy (MFM) [9,18,19], spin-polarized scanning tunneling microscopy (STM) [20] and transmission electron microscopy (TEM) [19,21,22]. TEM, the primary choice in this paper, can quantify local variations in magnetic field down to the nanometer scale using phase-sensitive methods such as Lorentz microscopy and electron holography.

In Lorentz microscopy, electrons subject to the Lorentz force are deflected sideways in opposite directions as they travel through regions of opposite magnetization [23]. This creates an observable image contrast along the domain walls. Among the family of Lorentz microscopy techniques, we select Fresnel imaging for our study. This method entails the acquisition of a set of defocused images where domain walls appear as bright or dark fringes. Lorentz microscopy can be carried out in-situ

\* Corresponding author.

E-mail address: [lasse.laurson@tuni.fi](mailto:lasse.laurson@tuni.fi) (L. Laurson).

<https://doi.org/10.1016/j.matchar.2026.116314>

Received 1 August 2025; Received in revised form 3 February 2026; Accepted 20 March 2026

Available online 21 March 2026

1044-5803/© 2026 The Authors. Published by Elsevier Inc. This is an open access article under the CC BY license (<http://creativecommons.org/licenses/by/4.0/>).

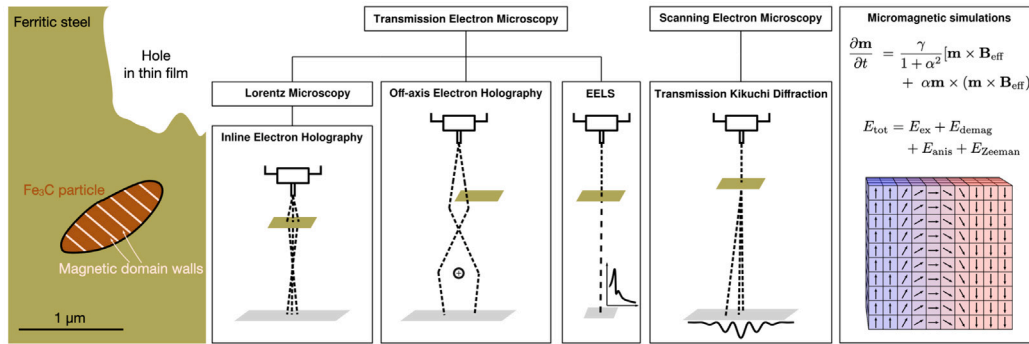


**Fig. 1.** The studied system consists of a cementite particle embedded in ferritic steel film. Various methods are used to characterize the microstructure and magnetic structure of the particle. Micromagnetic simulations are used to explain and verify the experimental results and analysis.

by controlling the magnetic flux density on the sample with a small excitation of the TEM objective lens.

Quantitative information on the local variations of magnetic induction and electrostatic potential in and around the sample [24] can be extracted from the phase of the electron wave function. In fact, the phase modulation of the electron wavefront emerging from the sample, called the exit wave, is linked to the electric and magnetic fields present as

$$\phi(\mathbf{r}) = C_E \int_z V(\mathbf{r}, z) dz - \frac{e}{\hbar} \int_z A_z(\mathbf{r}, z) dz, \quad (1)$$

where  $\mathbf{r} = (x, y)$  is the position vector in the sample plane,  $C_E$  is a constant depending on the acceleration voltage ( $C_E = 6.53 \text{ rad } \mu\text{m}^{-1} \text{ V}^{-1}$  at 300 kV), and  $V$  and  $\mathbf{A}$  are the electrostatic and magnetic potentials associated with the fields present within and around the sample.

Whereas Fresnel imaging is a phase contrast technique, where the observed image intensity variations are related differentially to the phase, electron holography (EH) [25] is a phase retrieval technique that measures the electron phase directly. The method relies on the formation of an interference pattern, the hologram, that carries phase information in the form of local fringe bending.

For any electrically unbiased and uncharged material, the electrostatic contribution to the phase shift reflects the average electrostatic potential of the atoms along the thickness of the specimen, commonly known as the mean inner potential (MIP). The MIP is the electron-optical equivalent of the refractive index in optics. In this case, Eq. (1) can be rewritten as

$$\phi(\mathbf{r}) = C_E V_{\text{MIP}}(\mathbf{r}) - \frac{e}{\hbar} \int_z A_z(\mathbf{r}, z) dz. \quad (2)$$

Off-axis electron holography employs a Möllenstedt biprism (a biased metallic wire) situated somewhere after the diffraction plane, most commonly in the selected area diffraction (SAD) plane. By applying a positive bias to the biprism, electrons are converged and, with enough coherence of the electron beam, they form an interference pattern. The complex valued exit-wave function of the electrons can be reconstructed from this fringe pattern using a Fast Fourier Transform based algorithm [26]. The phase shift is then extracted from the reconstructed exit wave to infer the electrostatic and magnetic properties of the sample according to Eq. (1).

Alternatively, the phase image can be retrieved by one of the in-line electron holography techniques: the transport-of-intensity equation (TIE) method [27–29]. TIE involves acquiring an in-focus image and a symmetric pair of over- and under-focused (Fresnel) images. The defocused images are used to approximate the derivative of the image intensity in the electron beam direction, which is then used as the source term of an inhomogeneous second-order partial differential equation involving the in-focus image intensity and the electron-optical

phase shift referenced to vacuum [28]. Here, we use TIE to accompany and benchmark our holographic measurements. These methods provide a microscopic view of the magnetization in real time that can be compared to theoretical models. Using different techniques helps to compare the method in case of infrastructure resources needed. Can other methods be used instead of resource-demanding off-axis holography and to which extend to gain similar information?

In parallel, we utilize micromagnetic simulations to support and explain the experimental results and analysis. Micromagnetic simulations constitute an accurate numerical description of magnetization and its dynamics on the intermediate scale between individual atoms, where quantum mechanical treatment is required, and the macroscopic scale. The key benefit of the method is its ability to resolve various magnetic structures such as domain walls and describe their dynamics. Micromagnetic simulations have been performed in the context of numerous applications ranging from nanoscale systems such as spintronics memory [9,30] and logic devices [5,31] to modeling the jerky field-driven motion of larger domain walls (up to a few micrometers in length) in disordered ferromagnets [32–34], i.e. the typical mechanism producing MBN. Here, we use the MuMax3 code [35], which solves the time and space dependent magnetization of a ferromagnetic body using a finite-difference discretization. To this end, the code solves numerically the Landau–Lifshitz–Gilbert equation [36],

$$\frac{\partial \mathbf{m}}{\partial t} = \frac{\gamma}{1 + \alpha^2} [\mathbf{m} \times \mathbf{B}_{\text{eff}} + \alpha \mathbf{m} \times (\mathbf{m} \times \mathbf{B}_{\text{eff}})] \quad (3)$$

on a finite-difference grid. Here,  $\mathbf{m}$  is a unit vector pointing in the direction of the magnetization,  $\gamma$  is the gyromagnetic ratio,  $\alpha$  is the Gilbert damping constant, and  $\mathbf{B}_{\text{eff}}$  is the effective field comprising of exchange, anisotropy, demagnetization and Zeeman field terms. Specific magnetic materials are modeled by choosing appropriate material-dependent values for the saturation magnetization  $M_s$ ,  $\alpha$ , the exchange stiffness  $A_{\text{ex}}$ , and the various anisotropy constants (uniaxial, cubic, etc.) altogether accounting for the diverse phenomenology of magnetic states, features, and responses to external stimuli.

Imaging methods and micromagnetic simulations each have their own limitations. Not all magnetic features can be visualized by microscopes (e.g. out of plane components). On the other hand, simulations cannot always reproduce all the experimentally observed phenomenology due to the lack of information on the material's defects or other experimental conditions that are hard to control.

In summary, we investigate the magnetic domain structures and their response to external magnetic fields of industrially relevant ferromagnetic steel, where the mechanical and magnetic properties are tuned by the presence of inherent cementite (Fe<sub>3</sub>C) carbide particles in a thin ferrite matrix. We obtain maps of magnetization through both the TIE approach and the in-situ off-axis electron holography to be compared with micromagnetic simulations. The target system and the methods used in this work are illustrated in Fig. 1.

The results provide unprecedented detailed views and models of these industrially important aspects of magnetization. The methodology can be applied to gain deeper insight in MBN and spintronic dynamics.

**Table 1**

Composition of steel determined by optical emission spectroscopy. The numbers are given in weight percent (%).

| Fe  | C   | Si  | Mn  | Cr  | Ni  | Cu  | P, S, Mo, Ti, V, Al, Nb, W |
|-----|-----|-----|-----|-----|-----|-----|----------------------------|
| Bal | 0.7 | 0.3 | 0.7 | 0.1 | 0.1 | 0.2 | < 0.1                      |

## 2. Materials and experimental methods

The materials, characterization methodologies, imaging methods, and setup of micromagnetic simulations are described in the following.

### 2.1. Material

Industrially relevant and commercially available hot-rolled steel with a ferritic–pearlitic structure was used. The steel composition (Table 1) was determined in Metlab Oy, Finland, by optical emission spectroscopy (OES).

### 2.2. Scanning electron microscopy imaging

The microstructure of the sample was studied with a scanning electron microscope (SEM, Zeiss Ultraplus) together with an electron backscatter diffraction (EBSD) system (Oxford Instruments Symmetry) enabling transmission Kikuchi diffraction (TKD) with higher spatial resolution compared to the ‘conventional’ EBSD measurements. The TKD data were collected with AZtec software and post-processed with Aztec-Crystal software (both from Oxford Instruments). A bulk sample for SEM studies was prepared with a conventional metallographic method: embedding in resin, followed by grinding, polishing, and etching with 4% Nital. A thin SEM-TKD sample, also used in the TEM studies, was prepared from mechanically pre-thinned (thickness < 100 μm) steel plate by machining a 3 mm diameter disc and then electropolishing (Struers TenuPol) the discs until perforation using a solution of nitric acid in methanol (1:3) at a temperature of −25 °C.

### 2.3. Coherent electron imaging

We map out the DWs by Fresnel imaging in an Environmental (Scanning) TEM (FEI Titan 80–300 kV E-(S)TEM) suitable for both inline and off-axis holography. As the incoming electrons interact with a domain, they are scattered to an angle determined by the Lorentz force acting on them. This interaction allows imaging the DWs, as the electron intensity around the DWs are either increased or decreased depending on the magnetization on either side of the DW, thereby creating visible contrast.

For a more quantitative analysis of the domain and DW structures we carried out electron holography experiments as the TEM is equipped with a standard ThermoFisher quartz filament biprism in the selected aperture plane and with a Gatan CMOS OneView camera for imaging with 4k sampling.

Our TEM is also equipped with a Gatan Imaging Filter (GIF) system (Gatan Tridiem 865 GIF) enabling electron energy loss spectroscopy (EELS) measurements. EELS was used to estimate the thickness of the sample in the region of interest (data not shown). In Lorentz microscopy, the strong 2 T magnetic twin-pole objective lens is switched off, and imaging is accomplished via a weaker Lorentz lens that leaves the sample in a field-free region. The downsides of the Lorentz lens are a lower magnification and a very large spherical aberration ( $C_s$ ). Combined, they produce a spatial resolution in the range of 5–10 nm. On the other hand, the magnetic field-free environment allows us to image magnetic samples non-invasively, without perturbing the magnetic structure under scrutiny.

In order to measure the phase shift using inline holography, the defocus is varied around the eucentric focus. We chose the following

set of defocus values:  $f = \pm 10, \pm 20, \pm 30, \pm 50, \pm 80, \pm 130, \pm 180, \pm 230, \pm 300, \text{ and } \pm 400 \mu\text{m}$ . In this mode, the microscopy was operated at low magnification at 9000 X and a dose rate of  $70 e^- \text{nm}^{-2} \text{s}^{-1}$ .

To setup off-axis electron holography, we first revert back to eucentric focus, and then bring in and turn on the biprism at some positive potential to create the interference pattern. At higher potentials, the electrons converge more, thereby creating both a larger interference region and reduced fringe spacing. However, a minimum fringe spacing is needed (around 4 pixels [26]) in order to effectively resolve fringes. In our experiments we kept the biprism voltage at 250 V, which resulted in 1.96 nm fringe spacing and 0.28 fringe contrast. To properly sample the interference fringes, the magnification was increased to 53 kX and the dose rate to  $50 e^- \text{\AA}^{-2} \text{s}^{-1}$ .

Following the standard off-axis electron holography acquisition procedure, two holograms were captured: the object hologram and background (vacuum) hologram. The latter is used to remove microscope distortions or any far field potentials as shown below in Section 2.4.

### 2.4. In-situ imaging

In both inline and off-axis modes the objective lens can be slightly excited to magnetize the sample. The objective twin-pole lens at maximum excitation produces a local magnetic field of 2 T, that can be directed as desired by tilting the sample appropriately.

The experimental protocol for in-situ imaging is as follows. We begin by aligning the microscope in normal Lorentz mode and acquire the hologram. Then, using free lens control, we slightly excite the objective lens to 1% (producing a field of 20 mT) and capture a second hologram. This is repeated in steps up to the maximum of 6% (120 mT) excitation. Afterwards, we reverse the objective lens current down to a minimum of −6% (−120 mT). Finally, the objective lens is brought back to 0% (0 mT) excitation. The microscope is realigned after every magnetic field increment, and the object/reference hologram pair is recorded each time.

We also captured videos of the domain wall dynamics while the objective lens was changing excitation. Since the current of the objective lens changed from frame to frame, the region of interest was slightly shifting at each step. Therefore, it was necessary to perform a post-alignment procedure by cross-correlation. In addition, denoising was applied for the aligned data. The aligning and denoising procedures that we adopted are described in Ref. [19].

### 2.5. Data analysis

All inline and off-axis holograms were processed via custom-made scripts, available in our Zenodo repository [37].

In off-axis electron holography, the interference pattern is created by superimposing the two portions of the exit wave passing on either side of the biprism. The portion that crosses the sample is termed object wave, while the other, traveling through vacuum only, is called reference wave. With planar illumination along the optic axis  $z$ , the exit wave has the form  $\psi = a \exp(izk_z + \phi(\mathbf{r}))$ , where  $a$  is the wave amplitude that is assumed constant, and  $\phi(\mathbf{r})$  is the phase modulation of the wavefront introduced by the electric and magnetic fields according to Eq. (1). By action of the biprism, the exit wave splits into object and reference, which are then brought to interfere. The hologram is the image intensity associated with this interference pattern, and can be written as

$$I(\mathbf{r}) = a_0^2 + a_r^2 + 2a_0a_r \cos(\mathbf{k}_c \cdot \mathbf{r} + \phi(\mathbf{r})) \quad (4)$$

showing that the phase shift is encoded in the hologram as local deviations from a pure sinusoidal pattern. In Eq. (4),  $a_0$  is the amplitude of the object wave,  $a_r$  the amplitude of the reference wave, and  $\mathbf{k}_c$  is the characteristic carrier frequency (the inverse fringe spacing) related to the angle of deflection of the biprism, which in turn connects to the biprism voltage and geometry.

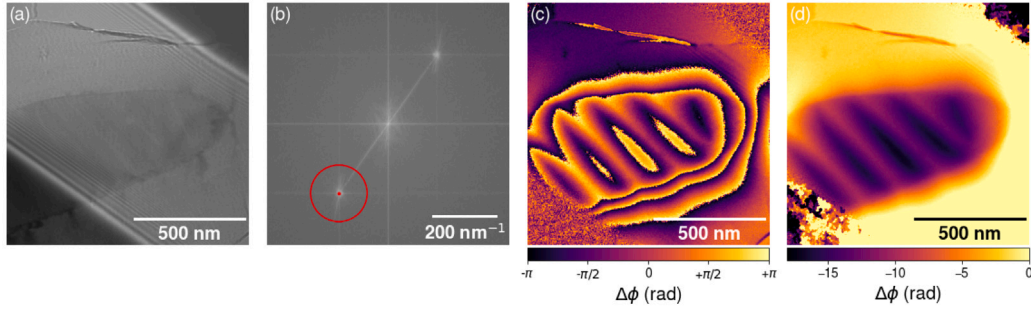


**Fig. 2.** Off-axis electron holography image analysis: (a) is the raw hologram, (b) its FFT and the applied mask on either of the two sidebands, (c) the reconstructed phase wrapped within the  $[-\pi; +\pi]$  interval, and (d) the unwrapped phase.

To measure the phase, the hologram is processed according to the standard fast Fourier transform (FFT) based reconstruction algorithm [26]. The reconstructed phase image from the algorithm is modulo  $2\pi$ , hence with discontinuities due to the indetermination of the  $\arg(\exp(i\phi))$  operation. It can be “unwrapped” by adding or subtracting  $2\pi$  at every discontinuity following a standard algorithm [38].

Fig. 2 shows an off-axis electron hologram of a carbide particle on the substrate together with the various terms involved in the reconstruction.

With inline holography, the phase can be retrieved by solving the TIE equation. Zuo et al. have written a comprehensive tutorial on the method [27], where the equation to solve can be written as [28,29]

$$\nabla \cdot [I(\mathbf{r}, 0) \nabla \phi(\mathbf{r})] = -\frac{2\pi}{\lambda_e} \frac{\partial I(\mathbf{r}, z)}{\partial z}, \quad (5)$$

with  $I(\mathbf{r}, 0) = a^2$  the in-focus TEM image,  $\lambda_e$  the relativistic wavelength of the electron wave (1.96 pm at 300 kV), and the axial derivative can be approximated as

$$\frac{\partial I(\mathbf{r}, z)}{\partial z} \approx \frac{I(\mathbf{r}, z+f) - I(\mathbf{r}, z-f)}{2f} \quad (6)$$

where  $f$  is the defocus distance measured from eucentric focus, that we set at  $z = 0$ . Choosing the appropriate defocus value can be challenging. For small  $f$  the defocused image intensities at the numerator in Eq. (6) may suffer excessively from noise. On the other hand, large jumps in  $f$  lead to the linear approximation of the gradient, Eq. (6), becoming poor. To ensure a proper sampling of the defocus range, we settled on the set of values mentioned in Section 2.3.

Assuming that the divergence of the amplitude ( $I(\mathbf{r}, 0) = |\psi(\mathbf{r})|^2 = a^2$ ) is constant, which is the case when dealing with pure phase objects featuring 100% transmittance, Eq. (5) can be rewritten and solved for  $\phi$  as

$$\phi(\mathbf{r}) = -\frac{\pi}{\lambda_e f} \nabla^{-2} \left[ \frac{I(\mathbf{r}, +f) - I(\mathbf{r}, -f)}{I(\mathbf{r}, 0)} \right] \equiv -\frac{\pi}{\lambda_e f} \nabla^{-2} [\bar{I}(\mathbf{r})] \quad (7)$$

where  $\nabla^{-2}$  represents the inverse Laplacian operator. Solving the reduced TIE (Eq. (7)) is best performed in Fourier space following the convolution theorem where the inverse Laplacian can be written as

$$\mathcal{F}(\nabla^{-2}) = -\frac{1}{4\pi^2 \mathbf{q}^2} \quad (8)$$

and hence the solution to the TIE, Eq. (7), can be written as

$$\phi(\mathbf{r}) = -\frac{1}{4\pi \lambda_e f} \mathcal{F}^{-1} \left\{ \frac{\mathcal{F}[\bar{I}(\mathbf{r})]}{\mathbf{q}^2} \right\}. \quad (9)$$

Prior to solving the TIE, the images are aligned so that the region of interest (ROI) overlaps between the various defocus values. This is to avoid artifacts in the reconstructed phase image as any misalignment will make  $\bar{I}(\mathbf{r})$  unreliable. For this alignment we use template matching: from the 0<sup>th</sup> image ( $z = 0$ ) we crop out an ROI that is used as a template for the other two images. The openCVs [39] Template Matching function allows us to quickly identify the ROI in each image and then

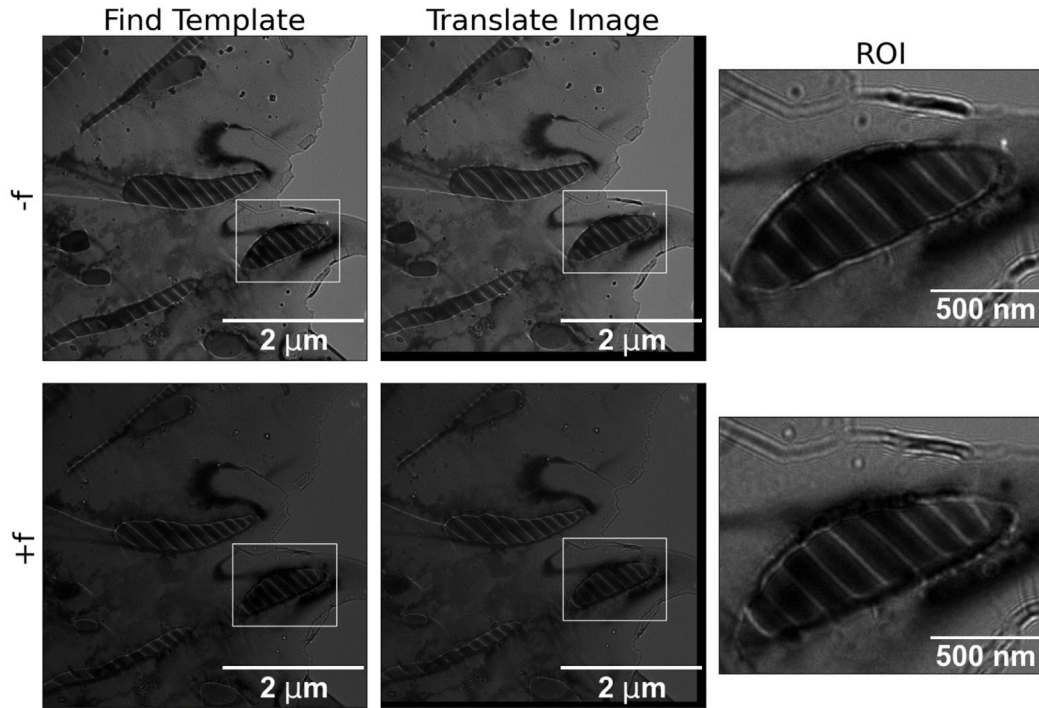
shift that image to align with the first. This was repeated for all images and defocus values (see Fig. 3). Note that this procedure assumes that the magnification is unchanged with defocus, as the algorithm does not rescale images. This approximation is reasonable when the defocus is kept small.

Fig. 4 shows the image processing that leads to the TIE reconstruction of the phase image of a carbide particle, summarizing the introduction to the TIE solution and its implementation in this work.

### 3. Simulation methods and setup

In this work, the micromagnetic simulations are performed using the MuMax3 code [35]. The simulated system consists of a cementite particle embedded in Fe matrix, corresponding to the particle targeted in Figs. 2, 3, and 4. The particle is modeled as an ellipsoid with axes of 1000 nm in length ( $x$ ), 420 nm in width ( $y$ ), and 80 nm in thickness ( $z$ ), mimicking the dimensions of the particle as observed by TEM as closely as possible. The thickness of the Fe surroundings is 21 nm as based on EELS measurements. The computational grid point widths are 1.5 nm, 1.5 nm, and 1.5 nm in  $x$ ,  $y$ , and  $z$  directions, respectively. The grid size is  $1024 \times 1024 \times 64$  voxels, corresponding to the physical system size of  $1536 \text{ nm} \times 1536 \text{ nm} \times 96 \text{ nm}$ . The computations involve periodic boundary conditions along  $x$  and  $y$ . The Fe matrix has saturation magnetization of  $1700 \text{ kA m}^{-1}$ , exchange stiffness of  $21 \text{ pJ m}^{-1}$ , and cubic anisotropy constant of  $48 \text{ kJ m}^{-3}$  [40]. The cementite particle has saturation magnetization of  $1200 \text{ kA m}^{-1}$  [41] and triaxial (orthorhombic) anisotropy constants of  $330 \text{ kJ m}^{-3}$ ,  $280 \text{ kJ m}^{-3}$ , and  $0 \text{ kJ m}^{-3}$  [42]. The anisotropy axes directions correspond to the easy axes, referring to the crystal orientations of both the matrix and the particle as obtained by TKD (see Fig. 5(d) in Section 4). The exchange stiffness of cementite is reported to have the value of  $8.7 \text{ pJ m}^{-1}$  [43,44], but during this work it was observed that the results with the value of  $1.5 \text{ pJ m}^{-1}$  agrees better with the experimental results. The effect of the exchange stiffness is discussed in detail along with the results. We note that the exchange length for cementite is either 3.1 nm (when using  $A_{\text{ex}} = 8.7 \text{ pJ m}^{-1}$ ) or 1.3 nm (for  $A_{\text{ex}} = 1.5 \text{ pJ m}^{-1}$ ). While the grid point width of 1.5 nm is in the latter case marginally larger than the exchange length, given the small difference between the two, we do not expect significant inaccuracies due to this in the simulations. Moreover, using smaller grid point widths would not be feasible for the large system considered here.

To determine the optimal magnetic domain size in the carbide particle, we run multiple relaxations of the magnetic configuration after initializing different numbers of alternating, evenly sized, antiparallel domains in the particle and record the total energy of the relaxed system; the configuration with the lowest total energy gives the optimal domain size. The external field is then increased along the  $z$  axis to investigate how the domain structure and domain wall width changes with the applied field.



**Fig. 3.** The alignment procedure: the template taken from the 0th image (find template) and the template aligned with the 0th image (translate image) in either  $-f$  (top row) or  $+f$  (bottom row), and finally the ROI used.

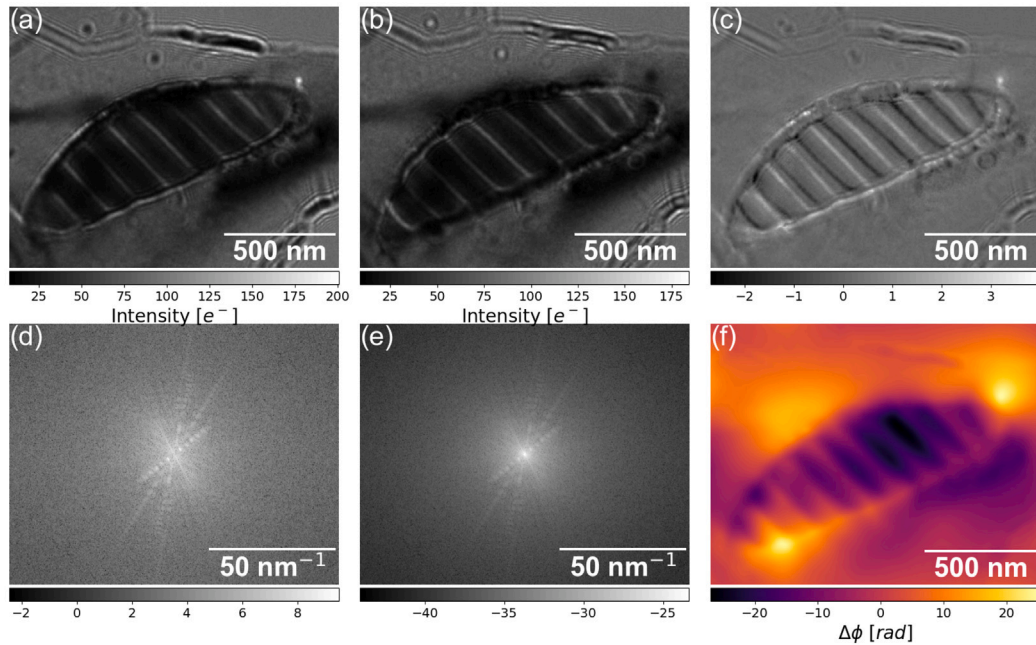


**Fig. 4.** Image analysis for inline holography at  $f = 180 \mu\text{m}$ , (a)  $z = -f$ , (b)  $z = +f$ , (c)  $\bar{I}(\mathbf{r})$  from Eq. (7), (d)  $\mathcal{F}[\bar{I}(\mathbf{r})]$ , (e)  $\mathcal{F}[\bar{I}(\mathbf{r})/q^2]$ , and (f) the phase image from Eq. (9).

To connect with the TEM data, we calculate the phase image from the results of the micromagnetic simulations according to the procedure in Ref. [45]. The phase map is obtained as

$$\phi(\mathbf{r}) = \frac{\pi\mu_0 t}{\phi_0} \mathcal{F}^{-1} \left( i(\tilde{M}_x k_y - \tilde{M}_y k_x) Q^2 \right) \quad (10)$$

where  $\mu_0$  is the vacuum permeability,  $t$  is the sample thickness,  $\phi_0 = h/2e$  is the flux quantum ( $h$  is Planck's constant, and  $e$  is the elementary

charge),  $M_x = M_s m_x$  is the  $x$  component of the local magnetization obtained from the micromagnetic simulations and  $\tilde{M}_x$  its Fourier transform,  $M_s$  is the local saturation magnetization, and  $Q = (k_x^2 + k_y^2)^{-1/2}$ . In the simulations, the thickness is not constant (see Fig. 9(a) for the geometry). Therefore, Eq. (10) is applied to each layer of the discretized simulation cell separately. The final total phase is then obtained as a sum over the layers, i.e. over the  $z$  coordinate of the system.

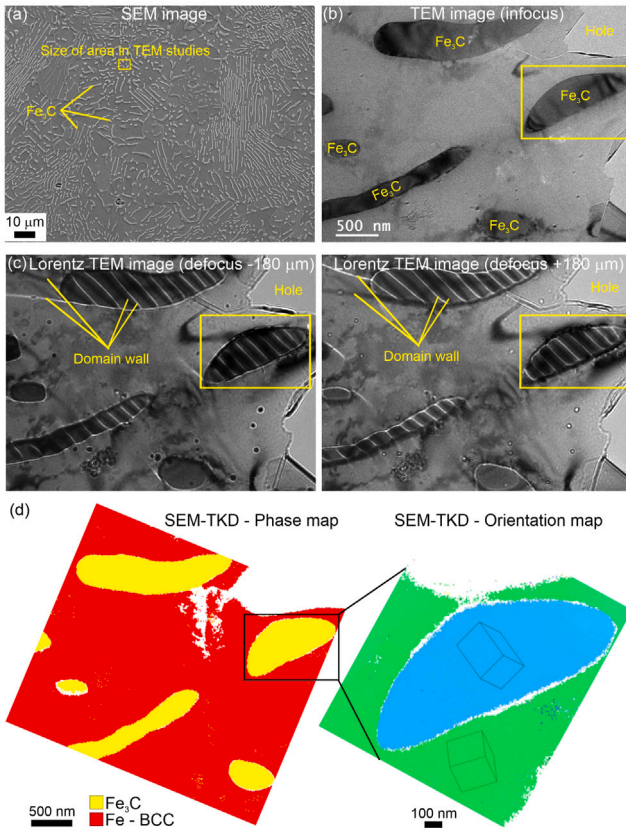


**Fig. 5.** Microstructure and magnetic structure of the sample, (a) SEM, (b) TEM, and (c) Lorentz TEM images together with (d) SEM-TKD phase map and orientation map with unit cells shows lamellar and spherical cementite ( $\text{Fe}_3\text{C}$ ) carbides in the ferritic matrix. In addition, there are domain walls in the matrix and inside the magnetic carbides. TEM image (b), Lorentz images (c), and SEM-TKD maps (d) are from the same area and the carbide studied is inside the yellow/black rectangle.

## 4. Results

### 4.1. Microstructure and magnetic structure

**Fig. 5** shows the results of SEM, TEM, Lorentz microscopy, and TKD studies. They indicate that the industrially relevant ferritic-pearlitic steel consists of lamellar and spherical cementite ( $\text{Fe}_3\text{C}$ ) carbides in the ferritic matrix. Based on the Lorentz images shown in **Fig. 5(c)**, there are domain walls both in the ferritic matrix and inside the magnetic cementite carbides. In this study, we focus on the approximately elliptical carbide as shown inside the yellow/black rectangles in **Figs. 5(b–d)**. Unit cells in the SEM-TKD orientation map, **Fig. 5(d)**, shows the crystal orientations of the carbide and ferritic matrix next to it. These orientations are used as input in the micromagnetic simulations.

### 4.2. Lorentz microscopy and off-axis electron holography

Examples of the phase maps measured with both in-line and off-axis electron holography methods are shown in **Fig. 6**. The maps show qualitatively similar results, possessing stripes in the area of the carbide and more slowly varying phase signal elsewhere. Recalling Eq. (2), we note that these maps still include the electrostatic potential on top of the magnetic one that is of our interest. We will present the details of the treatment of the electrostatic potential after describing the model function for the magnetic DWs inside the carbide.

To demonstrate the direct imaging of the DW dynamics, we offer Video 1 (Supplementary Material) as an animation of subsequent, stationary TEM images showing the domain wall dynamics in the matrix and inside two carbides, while varying the excitation of the objective lens. During the animation, the field is increased to the maximum, reversed to the minimum and stepped back to zero twice. In the matrix, the DWs start to move before the carbide is saturated, while in the carbides the DWs seem to disappear at some field value and reappear already before the zero field is reached again.

To understand and quantify the magnetic phase signal within the carbide, we use a simple model for the vector potential associated with the magnetic structure inside the carbide. We start with the standard description of the magnetization unit vector,  $\mathbf{m}$ , as it turns from  $+y$  to  $-y$  over a  $\sigma$ -wide DW with its center at  $x_0$ . This shape of a domain wall can be written as [46]

$$\mathbf{m} = \begin{bmatrix} \sin(\alpha) \operatorname{sech}\left(\frac{x-x_0}{\sigma}\right), \\ \tanh\left(\frac{x-x_0}{\sigma}\right), \\ \cos(\alpha) \operatorname{sech}\left(\frac{x-x_0}{\sigma}\right) \end{bmatrix} \quad (11)$$

where the angle  $\alpha$  corresponds to the type of wall:  $\alpha = 0$  is a Bloch wall with spins rotating in the  $(y, z)$  plane,  $\alpha = \pi/2$  is a Néel wall with spins rotating in the  $(x, y)$  plane, and  $0 < \alpha < \pi/2$  is a hybrid wall where spins rotate in a vertical plane  $\alpha$  degrees off the  $x$  axis.

Eq. (2) tells us that the phase is proportional to the vector potential component along the optic axis  $z$ , which by virtue of  $\mathbf{B} = \nabla \times \mathbf{A}$  relates to the  $x$  and  $y$  components of  $\mathbf{B}$  only. Assuming that the dimension of the carbide particle parallel to the DW is much larger than the DW width itself, we may neglect the stray field, and its return flux, generated by the magnetic charges at the particle edge. In the case of a Bloch wall, we then have

$$\phi(x) = \frac{eB_0 t}{\hbar} \int m_y(x) dx \quad (12)$$

where  $t$  is the particle thickness and  $B_0 = \mu_0 M_s$  is the material's saturation magnetization measured in Tesla. The integral in Eq. (12) is indefinite because the phase is determined only up to an arbitrary constant, meaning that we are free to choose its zero anywhere. With the magnetization unit vector as in Eq. (11), we obtain

$$\phi(x) = A\sigma \ln \left[ \cosh\left(\frac{x-x_0}{\sigma}\right) \right] + C \quad (13)$$

where  $A = \frac{eB_0 t}{\hbar}$  reflects the slope of the phase far from the DW, and  $C$  is an arbitrary phase offset. The particle thickness  $t$  is measured using STEM-EELS (data not shown), yielding a thickness of approximately 80 nm. In the analysis involving Eq. (13), we assume  $t$  to be constant and neglect the elliptical shape of the particle for simplicity.

As a final remark of the model, we discuss the treatment of the electrostatic potential. Since we are interested in rather local features of the phase map, i.e. DW widths and domain sizes, it is sufficient to make the assumption that the smoothly varying electrostatic background from the mean inner potential constitutes a linear contribution locally in the phase shift. Therefore, we account for the electrostatic background by adding a linear term  $kx$  in the model function (Eq. (13)) whose coefficient  $k$  is fitted along with the other variables. The full model function for a domain wall becomes

$$\phi(x) = A\sigma \ln \left[ \cosh\left(\frac{x-x_0}{\sigma}\right) \right] + kx + C \quad (14)$$

that takes into account the contribution of the electrostatic potential as the linear term, returning a more accurate value for the DW width  $\sigma$  when fitted to a phase profile.

We proceed with the determination of the DW widths and domain sizes for holography images obtained under vertical magnetic fields of varying magnitude as described in Section 3. First, the analyzed phase profile is selected; this is done manually for each image due to small differences in the alignment between the images. The region where the phase profile is considered is shown in **Fig. 6(a)** as the white dashed

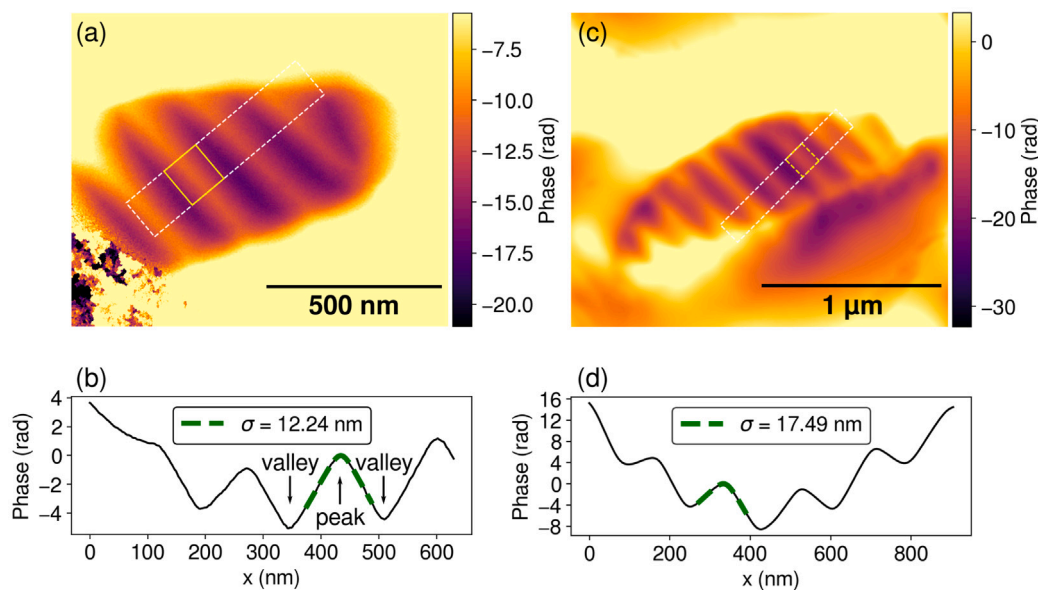


**Fig. 6.** (a) Example of a reconstructed phase map via off-axis electron holography. (b) The line profile inside the dashed rectangle shown in (a) together with a fit model function for a single peak, fitted inside the yellow rectangle shown in (a). (c) and (d): Similar data for inline holography and TIE analysis. In the phase maps, the color range is selected to highlight the structure inside the carbide particle.

rectangle. The analyzed phase profile is indicated in Fig. 6(b), where the 1-dimensional signal is taken as a mean over the region in the direction of the short axis of the rectangle in Fig. 6(a). The DW widths are determined by fitting Eq. (14) to a single peak in the phase signal, as shown in Fig. 6(b). The domain sizes are measured as peak-to-valley and valley-to-peak distances, that is the distances between the fitted peak to the valleys on its right and left sides, respectively.

The fit DW widths from Eq. (14) and the measured domain sizes are shown in Fig. 7(b) and (c) for each field value. The coloring and the analyzed field values are illustrated in Fig. 7(a). Starting from 0 mT, the DW width  $\sigma$  first rapidly collapses from 12 nm to 10 nm, then increases from 10 to 12 nm when the field is increased up to 120 mT. It then decreases back along the same path towards 0 mT. Below 0 mT, the trend is non-monotonous, and slight hysteresis can be seen while coming back from  $-120$  mT towards 0 mT. On the positive side of  $B$ , the monotonous, increasing trend can be understood by considering the energetics of Bloch walls. As the field is increased vertically, it becomes energetically favorable to expand the domain wall which aligns with the field, hence providing Zeeman energy relief. The trade-off between magnetostatic and exchange energies remains essentially unchanged, so that the net effect is a DW enlargement.

The domain sizes have more symmetric and non-hysteretic trend along the field loop than the widths, as shown in Fig. 7(c). The domain from valley to peak increases in size when the field becomes more positive, and, in the opposite, the domain from peak to valley decreases for more positive fields. This can be understood by the relationship between the anisotropy axes and the direction of the applied field. To simplify, let us consider a material with uniaxial anisotropy with easy axis direction  $\mathbf{u} = K_y\mathbf{y} + K_z\mathbf{z}$  with  $K_y, K_z > 0$ . Here, we have two mutually antiparallel domains, A and B, that have magnetization  $\mathbf{m}_A = a\mathbf{y} + b\mathbf{z}$  and  $\mathbf{m}_B = -a\mathbf{y} - b\mathbf{z}$  with  $a, b > 0$  and  $b \ll a$  because the sample is thin; the magnetization is close to in-plane configuration due to the shape anisotropy. Because of the symmetry of the anisotropy, these domains have the same energy. However, when the material is exposed to a vertical field  $\mathbf{B} = B_z\mathbf{z}$  with  $B_z > 0$ , the magnetization acquires a  $B_z$ -dependent positive  $z$  component. This decreases the anisotropy energy density in domain A and increases it in domain B, making domain A energetically more favorable and expanding it at the expense of B. The field with  $B_z < 0$  naturally has the opposite effect, expanding domain B.

The same methods carried out for the off-axis electron holography above are used for the TIE phase reconstruction, where the phase profile is acquired over approximately the same region. This is shown in Fig. 6(c) with an example of the analyzed curves shown in Fig. 6(d).

The TIE phase measurements confirm that the smaller defocus values ( $f < 80 \mu\text{m}$ ) lead to a poor signal-to-noise ratio (data not shown) and, consequently, to significant low-frequency artifacts in the signal. At the larger defocus values the profiles start to converge. Considering also that even the largest defocus values employed (up to  $400 \mu\text{m}$ ) are small compared to the Fresnel length of the DW ( $\lambda^2/4\lambda_e \sim 4 \text{ mm}$ ), we only compare TIE phase images obtained at  $f \geq 80 \mu\text{m}$  to the off-axis holographic results.

In Fig. 8(a), we show the width parameters  $\sigma$  for each defocus value. Here, the smallest defocus values where the signal-to-noise ratio is sufficiently large ( $f = 80 \mu\text{m}$ ), the fit  $\sigma$  is roughly the same as for off-axis holography at 0 mT although the fit has a relatively large standard error of about 1.4 nm. However, moving towards larger defocus values,  $\sigma$  jumps to 18 nm already at the next value  $f = 130 \mu\text{m}$  and slowly decreases when  $f$  is increased up to  $400 \mu\text{m}$ . Even though  $\sigma$  at  $400 \mu\text{m}$  shows rather good correspondence to the off-axis holography data, which we regard as the more accurate method of the two, we acknowledge that the fringe pattern emerging in the phase profile with such large defocus value introduces high uncertainty in the overall data. We expect that the smallest defocus values with sufficient signal-to-noise ratio gives the most trustworthy results. The domain sizes in Fig. 8(b) are of the same magnitude as for the off-axis holography, granting assurance that we are measuring the same thing (i.e. the electron phase) with both off-axis and inline holography. While both inline holography and TIE are valid phase retrieval methods, the latter requires a careful analysis to determine the sweet spot in defocus where the SNR is large enough but, on the other hand, where the small-defocus approximation underpinning the TIE formalism still holds.

The off-axis holography data and the fitted parameters are further combined to estimate the magnetic field inside the carbide particle that produces a 4–5 rad net phase shift, as shown in Fig. 6(a–b). Using the estimated thickness of 80 nm from STEM-EELS and the results of the fit for the A parameter, we find that  $B_0 \sim 0.5 - 0.6 \text{ T}$ . This is significantly smaller than the saturation magnetization of bulk cementite  $B_0 = 1.35 \text{ T}$  (Ref. [47]), suggesting that (i) the thickness estimated by EELS is flawed, (ii) not all the magnetic field is confined in the plane of the

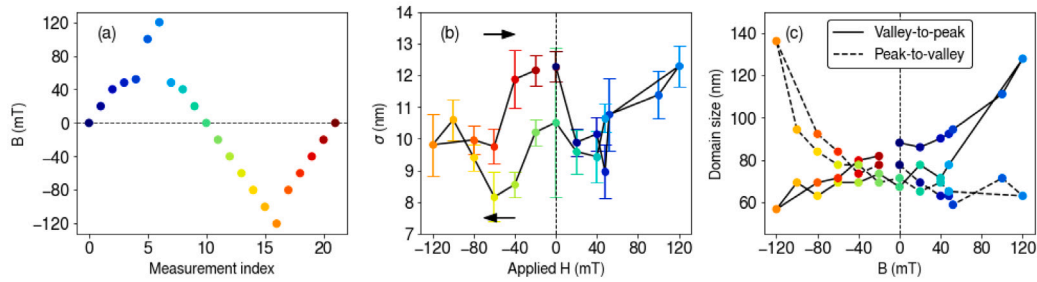


**Fig. 7.** (a) The applied field values corresponding to each subsequent acquisition of the data set. (b,c) The fitted parameters: (b) the DW thickness  $\sigma$  and (c) the domain size. Peak and valley refer to the respective features in the phase profile as illustrated in Fig. 6(b). The error bars are obtained as the square root of the self-covariance of the fit  $\sigma$ .

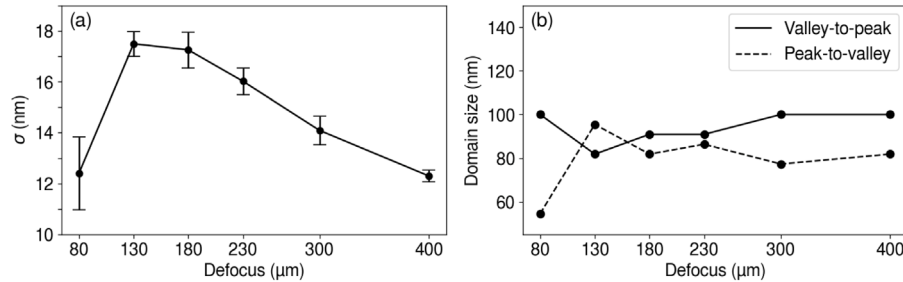


**Fig. 8.** The fitted parameters in the inline holography (TIE) data for different defocus values at zero field. (a) The domain wall widths  $\sigma$ . (b) The domain sizes.

particle, and (iii) the approximations we made of constant thickness, the DW shape as pure Bloch type, the model function, and the absence of stray fields (which reduce the net phase difference between DWs) were not so tenable after all.

#### 4.3. Micromagnetic simulation results

Here we present the results of our micromagnetic simulations, mimicking the experimental setup and the single carbide shown and analyzed in Figs. 2–8. We model the carbide particle as an ellipsoid, protruding from a thin film of iron as illustrated in Fig. 9(a). The motivations for choosing the geometry shown in Fig. 9(a) are two-fold: (i) the results obtained using it agreed slightly better with the experiments as compared to a carbide positioned perfectly symmetrically in the middle of the matrix, and (ii) it is unlikely that, following the etching process to make the sample thin, a thicker carbide would sit exactly symmetrically in the middle of the thin matrix. We compute the total energies of the system for different densities of in-carbide DWs and measure the DW widths. We vary the external field from 0 mT to +120 mT, down to -120 mT and back to 0 mT in 20 mT steps, relax the system at each field value, and analyze the DW evolution during this sequence of relaxations.

First, we resolve the optimal number of domains in the carbide that minimizes the total energy of the system. We initialize different number of DWs inside the carbide and relax the magnetic configuration afterwards. The resulting total energies are shown in Fig. 9(b) for two different values of the exchange stiffness: the literature value  $8.7 \text{ pJ m}^{-1}$  [43,44], and a smaller value of  $1.5 \text{ pJ m}^{-1}$  that we eventually found to match much better with the experimental data. The experimental data shows that the domain size is roughly 80 nm in zero field. In the simulations,  $A_{\text{ex}} = 8.7 \text{ pJ m}^{-1}$  results in optimal domain size of 166 nm (6 domains in particle of length 1000 nm), whereas the value of  $A_{\text{ex}} = 1.5 \text{ pJ m}^{-1}$  results in average domain size of 91 nm (11 domains). The latter matches well with the experimental observations. In Fig. 9(c), we show a three-dimensional illustration of the system with 11 domains in the carbide; the coloring denotes the magnetization directions on the surface. In addition to the domain structure of the

cementite carbide, consisting of roughly parallel 180 degree domain walls, in the Fe matrix surrounding the carbide, one can observe low-amplitude “waves” or oscillation patterns of the magnetization around the dominant in-plane magnetization direction of the Fe matrix, emanating from the domain structure of the carbide. This is similar to what is seen in the Lorentz microscopy images [Fig. 5(c)], where some domain wall-like structures appear to continue to the Fe matrix, with their contrast significantly weaker than that of the domain walls inside the carbides, suggesting that they do not correspond to 180 degree domain walls.

An interesting observation from the relaxation runs is that when 1–3 domains are initialized, some more DWs spontaneously emerge during the relaxation. This supports the experimental findings, demonstrated also in Video 1 (Supplementary Material), that the carbides very often show striped DW patterns by nature. Similarly, if more than 15 domains were initialized in the simulations, some of the domains vanished during the relaxation.

The value of  $A_{\text{ex}}$  thus matters a lot for the outcome. We also tested how changing the value of both saturation magnetization  $M_s$  and anisotropy constant  $K$  affects the number of domains that minimize the total energy. Using the literature value of  $A_{\text{ex}}$  and setting  $M_s = 2000 \text{ kA/m}$  results in 6 domains, and  $K_1 = 165 \text{ kJ/m}^3$ ,  $K_2 = 115 \text{ kJ/m}^3$ ,  $K_3 = 0 \text{ kJ/m}^3$  for the orthorhombic anisotropy constants results in 6 domains as well. That is, they do not have a significant effect on the optimal domain size, even though their spread reported in the literature values is rather large. Thus, even if the value  $A_{\text{ex}} = 1.5 \text{ pJ m}^{-1}$  is rather small, using such a small exchange stiffness seems to be the only way to reproduce the experimental domain patterns.

Hence, we continue the analysis with the value of  $A_{\text{ex}} = 1.5 \text{ pJ m}^{-1}$ . Figs. 10(a) and (b) show the relaxed magnetic structure and the converted phase map from the direction of the positive  $z$  axis, respectively. We note that the direction of DWs is slightly off from the elliptical axes of the particle, which is clearly visible e.g. in Fig. 4(c) and is repeated in the simulations: In Fig. 10(a), it can be seen that the domain walls are not exactly directed towards the short axis of the particle. In the figure, we have rotated the simulation box  $6^\circ$  in order to measure the domain wall width perpendicular to the domain wall direction. The inclination

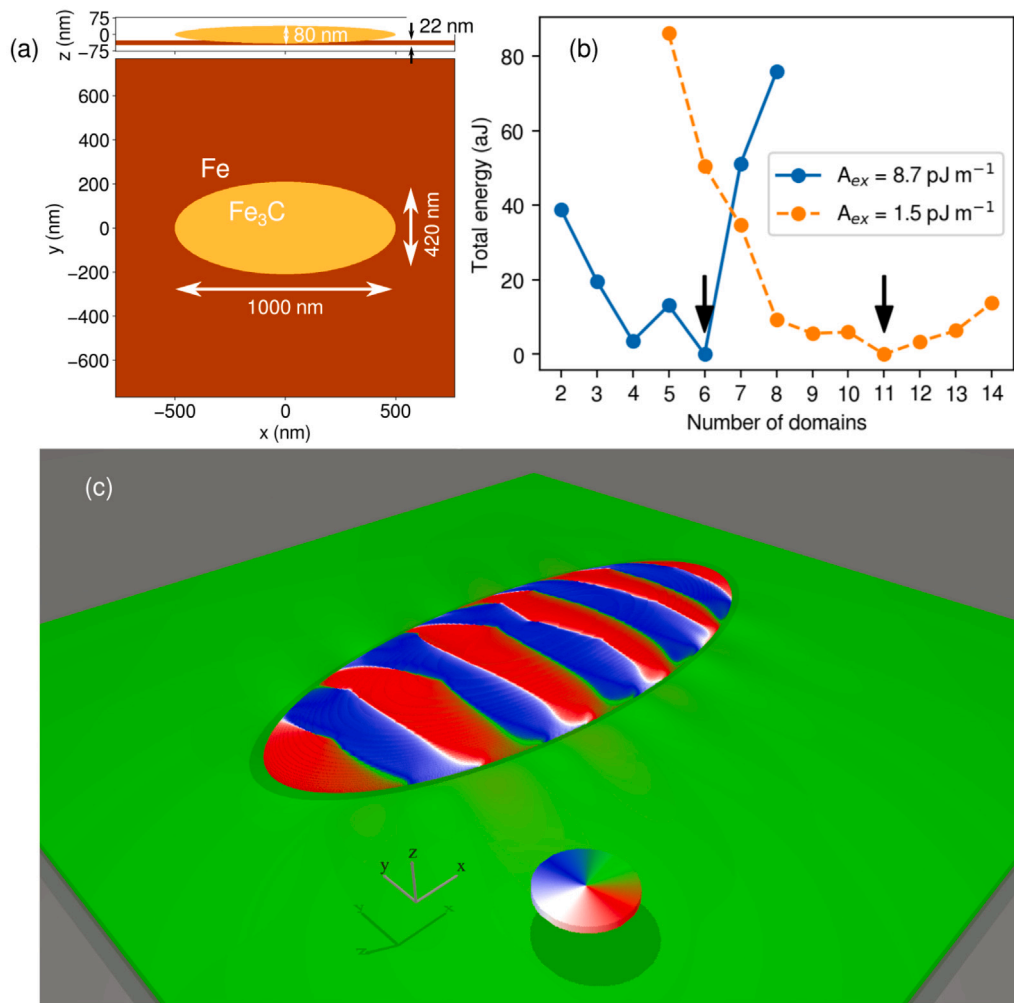


**Fig. 9.** (a) System geometry of the micromagnetic simulations. (b) Simulated total energies of systems with varying number of in-carbide domain walls. The values are shown for two different values of exchange stiffness:  $8.7 \text{ pJ m}^{-1}$  and  $1.5 \text{ pJ m}^{-1}$ . The smaller value for  $A_{\text{ex}}$  decreases the energy contribution of a DW. (c) Three-dimensional illustration of the relaxed magnetic state of the system. The coloring denotes the direction of the magnetization in  $(x, y)$  plane as indicated by the color wheel.

results from the magnetocrystalline anisotropy, which is mimicked in the simulations as accurately as possible using the easy axes from the measured TKD data.

We measure the DW widths in the measurement windows (Figs. 10 (a–b)) by both fitting the hyperbolic tangent on the DW shape ( $m_y$ , specifically) as shown in Fig. 10(c) and fitting with Eq. (14) in the simulated phase map as in Fig. 10(d) – as suggested in Section 4.2. The fitting with the tanh model function is performed on a curve that is taken as the average over both the  $y$  and  $z$  coordinates inside the measuring window, illustrated in Fig. 10(a). The fitting of the model function on the phase curve is taken as the average over the  $y$  coordinate inside the measuring window. The average over the  $z$  coordinate is weighted by the thickness and the  $M_s$  value as explained in the Methods section. The measured DW widths in the simulations at each value of the applied field  $H$  are shown in Fig. 10(e). The two methods show very similar trends in the  $\sigma$  evolution with the field, validating the experimental method of using the phase information as a tool to measure the domain wall width.

As a side note, we discuss the inclusion of the  $kx$  term in the model function for the simulated data even though the simulations do not involve any electrostatics. We include the  $kx$  term because there is slight skewness in the peaks of the phase curve, appearing because of the thin layer of Fe below the carbide particle. The domain structure

is partly transferred to Fe from the particle due to the exchange interaction between the two materials, but the structure is weaker in Fe. As a consequence, there is a net magnetization in the Fe layer towards its anisotropy axes, that contributes to a sloping part in the total phase profile. Including the  $kx$  term in the fitting function takes this effect into account and offers a more precise value for the DW width  $\sigma$ . The observation that the magnetization of the underlying Fe contributes to the slope of the phase, offers another reason to include the  $kx$  term in the analysis of the experimental data in addition to the electrostatic potential.

In Fig. 10(f), we plot the domain size evolution with the applied vertical field in the simulations. The picture is qualitatively the same as in the experiments: the more positive the field, the wider the valley-to-peak domain, and vice versa for the peak-to-valley domain. However, the range of domain sizes is a lot narrower as compared to experiments (10 nm vs. 70 nm) in the studied field range. Also, the valley-to-peak and peak-to-valley domains never reach each others' size unlike in experiments, where the curves meet at zero field. When using the literature value of  $A_{\text{ex}} = 8.7 \text{ pJ m}^{-1}$ , the domain size does not follow such a monotonous or easily interpreted behavior (data not shown), but the effect of increasing and decreasing the field is mostly to move the Bloch lines up and down along the domain walls. With  $A_{\text{ex}} = 8.7 \text{ pJ m}^{-1}$ , the domain sizes do not change very much, and their evolution

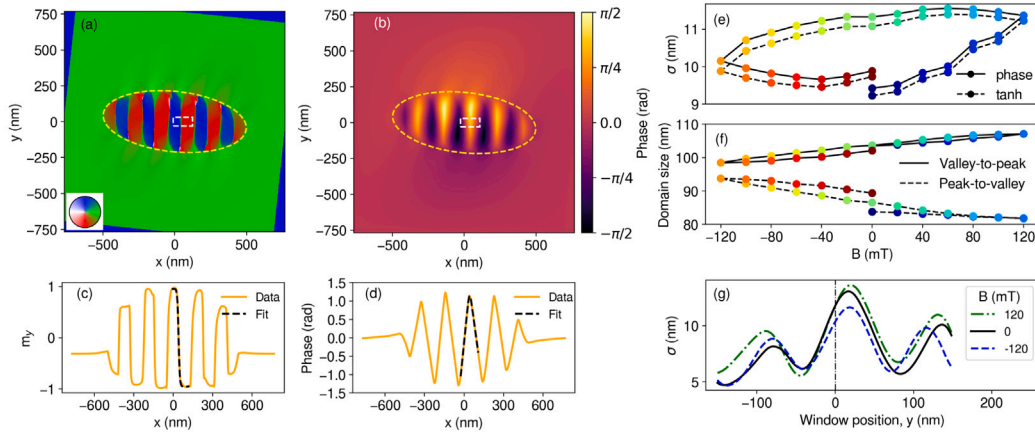


**Fig. 10.** Domain wall widths in simulations. (a) The system is relaxed after initializing 11 domain walls in the carbide. The coloring indicates the direction of the magnetization in  $xy$  plane. The yellow dashed ellipse indicates the boundary of the ellipsoidal cementite carbide. The white dashed rectangle shows the measuring window for the domain wall widths. (b) The phase map as converted from the simulated data. (c) Example of a hyperbolic tangent fit to the simulated magnetization data. The “tanh” curve is computed by fitting a function  $f(x) = D \tanh((x - x_0)/\sigma)$  to  $m_y$  in the measuring window in (a). (d) Example of a fit to the simulated phase data. The fit curve is computed by fitting model function, Eq. (14) to phase in the measuring window in (b). (e) The evolution of the simulated DW width parameter  $\sigma$  with varying external field. (f) The respective domain sizes. (g) The variance of the domain wall width by moving the measurement window along the  $y$  coordinate, i.e. along the domain wall in (a). The widths are measured by fitting to the tanh function here.

is counterintuitive at some field ranges: both the valley-to-peak and peak-to-valley domains increase with increasing the field. This gives us another reason to assume that  $A_{\text{ex}} = 1.5 \text{ pJ m}^{-1}$  is closer to the real, effective value in the microscopy experiments.

According to the simulated data, the domain wall width  $\sigma$  shows strong hysteretic behavior when the applied field is driven up and down. The shape of the behavior is qualitatively very different than the experimental measurements (Fig. 7(b)), but the range of the domain wall widths stays between 9 and 12 nm that is consistent with the experiments. We attribute the differences in the shape to the challenge of determining a unique value for the domain wall width in such particles. For example, in Fig. 10(g) we show how moving the measurement window along the  $y$  axis changes the outcome of the measurement for a single DW. The width parameter  $\sigma$  changes between 5 and 14 nm, showing a remarkable effect of the window position on the measurement. A detailed inspection of the magnetization data reveals that there are Bloch lines within the DWs that move slightly up and down when the field magnitude is changed, influencing the DW width. We illustrate this in Video 2 (Supplementary Material), where the meeting points of white and black regions ( $m_z < 0$  and  $m_z > 0$ , respectively) of the DW represent Bloch lines. When the Bloch line enters the measurement window, the measured DW width is larger than elsewhere. For example, each curve in Fig. 10(g) contains three peaks. In Video 2, we see that there is a Bloch line in the described DW at the position of each peak. It is thus clear that the presence of Bloch lines makes the measured  $\sigma$  larger.

The DW widths measured with both the off-axis electron holography in Fig. 7(b) and the micromagnetic simulations are larger than what the theoretical, simplified Bloch wall formulation  $w = \sqrt{A/K} = 2.1 \text{ nm}$  predicts. To offer an explanation for this using the simulated data, in Fig. 11 we show the widths and positions of a domain wall along the  $z$  axis. The measurement window is the same as shown in Fig. 10(a). Fig. 11(a) shows that the DW has a relatively constant width ( $\sim 5 \text{ nm}$ ) inside the carbide. Inside the thin layer of Fe below the carbide, the width is larger, because there is no anisotropy direction supporting such a DW in the underlying Fe; The DW only exists there due to the exchange coupling with the carbide. Fig. 10(b) explains the deviance of the widths from the theory: the DW is tilted inside the carbide, and therefore the width that is averaged over the thickness seems larger than the theoretical prediction. The difference between the measured  $\sigma$  for 120 mT and  $-120 \text{ mT}$  (Fig. 10(e)) can be explained only by

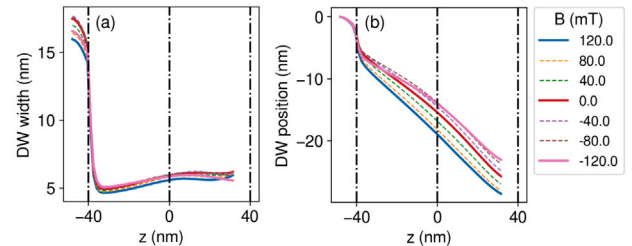


**Fig. 11.** (a) The domain wall widths and (b) relative positions in  $x$  direction along the thickness ( $z$  axis) of the carbide for different magnitudes of the applied field, where  $z = 0$  is the midpoint of the carbide particle. The values for the width ( $\sigma$ ) and position ( $x_0$ ) are obtained from fitting the domain wall shape grid layer by grid layer to the function  $f(x) = D \tanh((x - x_0)/\sigma)$ . The dashed dotted lines show the bottom, middle level, and top of the carbide. Below  $z = -40 \text{ nm}$  there is a thin layer of Fe (see Fig. 9(a) for the geometry). In (b), the curves are offset to align the domain wall position at the first measured grid layer. The position curves indicate that the domain wall is tilted inside the carbide, effectively broadening the wall while measuring it by averaging over the thickness.

the changes in the tilting of the DW: at  $-120 \text{ mT}$ , the DW is a little more straight than at  $+120 \text{ mT}$ , decreasing the measured value that is averaged over the thickness.

As a finishing note of the micromagnetic results, the domain wall widths are also examined with the exchange stiffness value  $A_{\text{ex}} = 8.7 \text{ pJ m}^{-1}$ . Despite the different optimal domain sizes, there is no substantial difference in the domain wall widths as compared to the ones presented above for the literature value  $A_{\text{ex}} = 1.5 \text{ pJ m}^{-1}$ . In both cases, the DWs are tilted and inclined, Bloch lines are formed spontaneously, and the DW widths depend on the measurement window position.

## 5. Discussion

We begin the theory-oriented explanation of the experimental results by arguing with energy consideration why the stripe domain wall structure is formed in the carbides. As per Fig. 5(d), the magnetocrystalline anisotropy axes are directed in such a way that the hard axis of cementite is roughly along the long edge of the ellipsoidal particle. In typical soft or low-anisotropy magnetic particles, the Landau pattern

with a centered vortex is formed in order to minimize the energy stored in the magnetostatic field outside the particle (i.e. the stray field). Due to the strong magnetocrystalline anisotropy of cementite [42], the typical Landau pattern is here energetically expensive. In contrast, the stray field energy is decreased by formation of multiple alternating, antiparallel domains that result in only small domain closure patterns outside the particle. The optimal domain size results from the competing energy factors: increasing the number of domains decreases the stray field energy but increases the number of domain walls that each increase the total energy. Thus, we attribute the appearance of the edge-to-edge domain walls to the strong magnetocrystalline anisotropy in cementite.

According to the domain size analysis shown in Fig. 7(c), the domain size is close to 80 nm at zero field. In the simulations with the literature value  $8.7 \text{ pJ m}^{-1}$  for  $A_{\text{ex}}$ , the energy-minimizing domain size is 166 nm. Decreasing the exchange stiffness  $A_{\text{ex}}$  to a sixth of the literature value ( $1.5 \text{ pJ m}^{-1}$ ), the average domain size is roughly 91 nm which is much closer to the TEM observations. However, there might also be different reasons why the smaller  $A_{\text{ex}}$  leads to results closer to the experiments. Firstly, to our knowledge, the value of the exchange stiffness is not very well validated, but the estimated value that we take from the literature is only based on the Curie temperature of cementite [43,44]. Secondly, the temperature in the experiments is of the order of 300 K, whereas the micromagnetic parameters are determined for zero temperature; increased temperature tends to weaken the exchange coupling in a complicated fashion [48], and therefore it is possible that the effective exchange stiffness of  $\text{Fe}_3\text{C}$  is closer to  $1.5 \text{ pJ m}^{-1}$  than to  $8.7 \text{ pJ m}^{-1}$  at 300 K. Our observations of the domain size evolution with the applied field supports the use of  $A_{\text{ex}} = 1.5 \text{ pJ m}^{-1}$  as well, as the results correspond to the experimental observations more than those with  $A_{\text{ex}} = 8.7 \text{ pJ m}^{-1}$ .

The domain wall widths and their evolution with the applied field match well with the experiments. The measured domain wall width is 8–12 nm in both simulations and experiments, even though the simulations show that the measurement window position has a notable effect on the obtained results. While the width range exceeds the theoretical value of 2.1 nm for a pure Bloch wall, as we discussed, the tilting of the domain wall throughout the thickness of the particle makes the measured width even larger than what it is in the  $xy$  cross section of the particle. The changes in the tilting with the applied field can be related to the internal structure of the DWs and, in particular, Bloch lines within the DWs and their response to the field. Bloch lines are spontaneously formed in the DWs, and the vertical field makes them move up and down along the DW. It is observed that the DW width is enlarged in the vicinity of the Bloch line. This is why a unique value for the DW width cannot be determined, as it depends on the selected measurement window where the analysis is performed and the positions of the Bloch lines. Regarding the experimental analysis, the comparison of the tanh and phase fitting treatments for the simulated data suggests that the phase retrieval methods can be used to recognize Bloch lines in the microscopy data.

The consistency between the two holography methods (inline and off-axis) indicates that both can be used to map out magnetic properties of a magnetic sample (ferromagnetic or not), at least in a semi-quantitative fashion. Each comes with their own drawbacks. Inline electron holography is time consuming as it requires at least 3 images at each experimental condition, the TIE reconstruction algorithm is more demanding and user-choice-dependent, and the quantification is not only dependent on image quality but also on how accurately the defocus is known. On the positive side, most TEMs are equipped by default to carry out inline electron holography. Even if a Lorentz lens is not present, viable imaging conditions can be found in free lens control with the objective lens turned off, although resolution might be limited.

On the other hand, off-axis electron holography is only possible with an electron biprism and, therefore, it is more costly. However, acquisition is faster as it only requires a single image (the object

hologram) and a global reference hologram for each data set to remove far-field distortions. Alignment of the electron biprism is a bit more tricky compared to ordinary TEM alignment as the object and reference waves need to correctly overlap in order to obtain a suitable interference pattern with sufficient coherence. Finally, image analysis is less cumbersome than TIE, as it does not involve differential operators. Similar conclusions have been drawn by T. Latychevskaia et al. [49].

Both methods, however, present some challenges in providing accurate measurements of the physical quantities relevant for the analysis and interpretation. For example, the value of the magnetic field might be uncertain as it is estimated based on the percentage of the full power of the objective lens and on external calibration. For small fields, however, the error is typically less than 10% [22]. In the TIE analysis, the accurate knowledge of the defocus value is crucial to produce quantitatively correct results, which also requires a non-trivial calibration of the whole microscope in the exact same experimental conditions used.

## 6. Conclusions

Electron holography adds to the value of Lorentz imaging by allowing nanometer-resolution determination of the domain wall widths and the magnetic parameters of thin film samples with varying external fields. We have used both inline and off-axis electron holography to study the domain and domain wall structures in cementite carbides, where the strong anisotropy enforces the magnetic configuration in a regular striped pattern. Our results indicate that the off-axis holography provides results for magnetic domain and domain wall characteristics with varying vertical field that match with the theory-based simulations. The inline holography shows more ambiguous results in that there is no clear trend from the smallest defocus value towards the larger ones. The qualitative picture of the TIE analysis is reasonable, nevertheless. The cementite carbide particles show stable domain wall structure at least up to  $H = 120 \text{ mT}$ . The analysis of the holographic data suggests a value for the saturation magnetization  $M_s$  of cementite to be 0.5 – 0.6 T, which is around half of the literature value. We attribute this deviance to the various assumptions and approximations done in our analysis, suggesting that the method to determine  $M_s$  for an ellipsoidal particle that protrudes from a thin film is not very practical after all.

With the essential magnetocrystalline anisotropy information obtained from the SEM-TKD characterization of the carbides, the micromagnetic simulations were successfully used to explain the appearance and directionality of the stripe pattern of domain walls in the cementite carbide, embedded in the thin iron film. The simulations were also used to explain the holography-based DW widths and their deviation from the theoretical Bloch wall result as well as the evolution of the domain wall width with the varying external field. The simulated data was successfully converted to corresponding phase information that is obtained through both inline and off-axis electron holography. According to the micromagnetic simulations, Bloch lines are formed in the domain walls within the carbide. This suggests that the domain wall width might not have a well-defined, unique value even as measured in the holography experiments. The credibility of the micromagnetic simulations is challenged by the uncertainty of the material parameters for cementite, as discussed in Section 4.3. Especially, the value of exchange stiffness was observed to have a major effect on the optimal domain size in the simulations, while there is uncertainty in its literature value and it needs more accurate determination for more reliable results. Our key contribution here is to point out that using the literature values for the micromagnetic parameters of cementite fails to reproduce the experimental domain patterns, and that by adjusting  $A_{\text{ex}}$  one can tune the numerical domain pattern to become closer to the experimental ones. This highlights the need for further studies of this issue.

Micromagnetic simulations offer valuable insight into the internal DW structure that is challenging to approach via Lorentz microscopy

or electron holography. For example, the Bloch lines are more or less invisible to the microscope. However, the tilting of the domain walls in the thickness direction of the sample could, in principle, be assessed by tilting the sample inside TEM and recording a series of domain wall widths as a function of the tilting angle.

Electron holography can thus be fruitfully employed to explore the magnetic structures with nanometer resolution. In spintronics, it can be used to validate the behavior of domain walls with varying external fields in a device with defects (whether intended or not). In magnetic Barkhausen noise research, electron holography could be employed to provide detailed information on the domain and domain wall structures at the grain boundaries, interfaces, or in the vicinity of dislocations. Both of these utilization areas would benefit from detailed information gained with characterization to understand the theoretical background of industrial measurements and to evaluate better results from different end-user cases. We also anticipate that electron holography could be used to resolve various magnetic parameters in addition to the saturation magnetization. For example, the exchange stiffness of a material could be determined based on the domain wall type (Bloch or Néel), widths, and tilting fraction once the uniaxial magnetocrystalline anisotropy constant is well-defined. This study suggests that the resource-demanding off-axis holography can, to some extent, be substituted by the less demanding inline holography and the related transport of intensity equation which, however, requires more manual work at the microscope and parameter choices by the user. The yet under-investigated opportunities of phase retrieval in TEM studies deepens our understanding of the magnetic behavior and response to external fields of ferromagnetic materials, thus advancing the development of spintronic devices and research on magnetic Barkhausen noise for more sustainable and energy-efficient future technologies.

#### CRedit authorship contribution statement

**Sami Kaappa:** Writing – original draft, Visualization, Software, Methodology, Investigation, Formal analysis, Data curation, Conceptualization. **Mads Søndergaard Larsen:** Writing – original draft, Visualization, Software, Methodology, Investigation, Formal analysis, Conceptualization. **Suvi Santa-aho:** Writing – original draft, Visualization, Methodology, Investigation, Data curation, Conceptualization. **Murat Nulati Yesibolati:** Writing – review & editing, Visualization, Investigation. **Mari Honkanen:** Writing – original draft, Visualization, Supervision, Project administration, Methodology, Investigation, Funding acquisition, Data curation, Conceptualization. **Kristian Speranza Mølhave:** Writing – review & editing, Supervision. **Minnamari Vippola:** Writing – review & editing, Supervision, Project administration, Funding acquisition, Conceptualization. **Lasse Laurson:** Writing – original draft, Visualization, Supervision, Software, Project administration, Methodology, Investigation, Funding acquisition, Formal analysis, Data curation, Conceptualization. **Marco Beleggia:** Writing – original draft, Visualization, Supervision, Software, Methodology, Investigation, Formal analysis, Conceptualization.

#### Funding

This work was supported by Research Council of Finland [grant numbers 338954, 338955].

#### Declaration of competing interest

The authors declare that they have no known competing financial interests or personal relationships that could have appeared to influence the work reported in this paper.

#### Acknowledgments

SEM work made use of Tampere Microscopy Center facilities (Tampere University, Finland). Both inline and off-axis electron holography made use of the Environmental TEM at DTU Nanolab (Technical University of Denmark, Denmark). The authors acknowledge the computational resources provided by CSC, IT Center for Science Ltd. (Finland). We would like to thank PhD Monia R. Nielsen (Technical University of Denmark) for her help on the E-TEM related to STEM-EELS thickness measurements, PhD Lucio Azzari (Tampere University) for his effort on the video frame editing, and B.Sc. Justus Rantala (Tampere University) for his assistance in the sample preparation.

#### Appendix A. Supplementary data

Supplementary material related to this article can be found online at <https://doi.org/10.1016/j.matchar.2026.116314>.

#### Data availability

Data will be made available on request.

#### References

- [1] J. Puebla, J. Kim, K. Kondou, Y. Otani, Spintronic devices for energy-efficient data storage and energy harvesting, *Commun. Mater.* 1 (1) (2020) 24, <http://dx.doi.org/10.1038/s43246-020-0022-5>.
- [2] Z. Guo, J. Yin, Y. Bai, D. Zhu, K. Shi, G. Wang, K. Cao, W. Zhao, Spintronics for energy-efficient computing: An overview and outlook, *Proc. IEEE* 109 (8) (2021) 1398–1417, <http://dx.doi.org/10.1109/JPROC.2021.3084997>.
- [3] G. Finocchio, M. Di Ventra, K.Y. Camsari, K. Everschor-Sitte, P. Khalili Amiri, Z. Zeng, The promise of spintronics for unconventional computing, *J. Magn. Magn. Mater.* 521 (2021) 167506, <http://dx.doi.org/10.1016/j.jmmm.2020.167506>.
- [4] A. Fert, R. Ramesh, V. Garcia, F. Casanova, M. Bibes, Electrical control of magnetism by electric field and current-induced torques, *Rev. Modern Phys.* 96 (2024) 015005, <http://dx.doi.org/10.1103/RevModPhys.96.015005>.
- [5] Z. Luo, A. Hrabec, T.P. Dao, G. Sala, S. Finizio, J. Feng, S. Mayr, J. Raabe, P. Gambardella, L.J. Heyderman, Current-driven magnetic domain-wall logic, *Nature* 579 (7798) (2020) 214–218, <http://dx.doi.org/10.1038/s41586-020-2061-y>.
- [6] D.A. Allwood, G. Xiong, C.C. Faulkner, D. Atkinson, D. Petit, R.P. Cowburn, Magnetic domain-wall logic, *Science* 309 (5741) (2005) 1688–1692, <http://dx.doi.org/10.1126/science.1108813>.
- [7] E. Raymenants, O. Bultynck, D. Wan, T. Devolder, K. Garello, L. Souriau, A. Thiam, D. Tsvetanova, Y. Canvel, D.E. Nikonov, I.A. Young, M. Heyns, B. Soree, I. Asselberghs, I. Radu, S. Couet, V.D. Nguyen, Nanoscale domain wall devices with magnetic tunnel junction read and write, *Nat. Electron.* 4 (6) (2021) 392–398, <http://dx.doi.org/10.1038/s41928-021-00593-x>.
- [8] J. Godinho, P.K. Rout, R. Salikhov, O. Hellwig, Z. Šobán, R.M. Otxoa, K. Olejník, T. Jungwirth, J. Wunderlich, Antiferromagnetic domain wall memory with neuromorphic functionality, *Npj Spintron.* 2 (1) (2024) 39, <http://dx.doi.org/10.1038/s44306-024-00027-2>.
- [9] S.S. Parkin, M. Hayashi, L. Thomas, Magnetic domain-wall racetrack memory, *Science* 320 (5873) (2008) 190–194, <http://dx.doi.org/10.1126/science.1145799>.
- [10] D. Kumar, T. Jin, S. Al Risi, R. Sbiaa, W.S. Lew, S.N. Piramanayagam, Domain wall motion control for racetrack memory applications, *IEEE Trans. Magn.* 55 (3) (2019) 1–8, <http://dx.doi.org/10.1109/TMAG.2018.2876622>.
- [11] D. Kumar, T. Jin, R. Sbiaa, M. Kläui, S. Bedanta, S. Fukami, D. Ravelosona, S.-H. Yang, X. Liu, S.N. Piramanayagam, Domain wall memory: Physics, materials, and devices, *Phys. Rep.* 958 (2022) 1–35, <http://dx.doi.org/10.1016/j.physrep.2022.02.001>.
- [12] T. Le Manh, J.A. Pérez Benitez, J.H. Espina Hernández, J.M. Hallen López, Barkhausen Noise for Nondestructive Testing and Materials Characterization in Low-Carbon Steels, Woodhead Publishing, 2020.
- [13] G. Durin, S. Zapperi, The Barkhausen effect, in: G. Bertotti, I. Mayergoyz (Eds.), *in: The Science of Hysteresis, vol. II, Elsevier, Amsterdam, 2006, pp. 181–267*.
- [14] M. Al Bahri, B. Borie, T.L. Jin, R. Sbiaa, M. Kläui, S.N. Piramanayagam, Staggered magnetic nanowire devices for effective domain-wall pinning in racetrack memory, *Phys. Rev. Appl.* 11 (2019) 024023, <http://dx.doi.org/10.1103/PhysRevApplied.11.024023>.

- [15] T. Jin, D. Kumar, W. Gan, M. Ranjbar, F. Luo, R. Sbiaa, X. Liu, W.S. Lew, S.N. Piramanayagam, Nanoscale compositional modification in Co/Pd multilayers for controllable domain wall pinning in racetrack memory, *Phys. Status Solidi (RRL) – Rapid Res. Lett.* 12 (10) (2018) 1800197, <http://dx.doi.org/10.1002/pssr.201800197>.
- [16] J. Liu, G.Y. Tian, B. Gao, K. Zeng, Y. Zheng, J. Chen, Micro-macro characteristics between domain wall motion and magnetic Barkhausen noise under tensile stress, *J. Magn. Magn. Mater.* 493 (2020) 165719, <http://dx.doi.org/10.1016/j.jmmm.2019.165719>.
- [17] M. Al Bahri, B. Borie, T.L. Jin, R. Sbiaa, M. Kläui, S. Piramanayagam, Staggered magnetic nanowire devices for effective domain-wall pinning in racetrack memory, *Phys. Rev. Appl.* 11 (2) (2019) 024023, <http://dx.doi.org/10.1103/PhysRevApplied.11.024023>.
- [18] D. Kumar, T. Jin, S. Al Risi, R. Sbiaa, W.S. Lew, S. Piramanayagam, Domain wall motion control for racetrack memory applications, *IEEE Trans. Magn.* 55 (3) (2018) 1–8, <http://dx.doi.org/10.1109/TMAG.2018.2876622>.
- [19] S. Santa-aho, M. Honkanen, S. Kaappa, L. Azzari, A. Saren, K. Ullakko, L. Laurson, M. Vippola, Multi-instrumental approach to domain walls and their movement in ferromagnetic steels—origin of Barkhausen noise studied by microscopy techniques, *Mater. Des.* 234 (2023) 112308, <http://dx.doi.org/10.1016/j.matdes.2023.112308>.
- [20] R. Wiesendanger, *Atomic-and Nanoscale Magnetism*, Springer, 2018.
- [21] I. Manke, N. Kardjilov, R. Schäfer, A. Hilger, M. Strobl, M. Dawson, C. Grünzweig, G. Behr, M. Hentschel, C. David, et al., Three-dimensional imaging of magnetic domains, *Nat. Commun.* 1 (1) (2010) 125, <http://dx.doi.org/10.1038/ncomms1125>.
- [22] M. Honkanen, H. Lukinmaa, S. Kaappa, S. Santa-Aho, J. Kajan, S. Savolainen, L. Azzari, L. Laurson, M. Palosaari, M. Vippola, Magnetic domain wall dynamics studied by in-situ Lorentz microscopy with aid of custom-made hall-effect sensor holder, *Ultramicroscopy* 262 (2024) 113979, <http://dx.doi.org/10.1016/j.ultramic.2024.113979>.
- [23] R.E. Dunin-Borkowski, T. Kasama, M. Beleggia, G. Pozzi, Lorentz microscopy and electron holography of magnetic materials, *Handb. Nanoscopy* (2012) 221–251, <http://dx.doi.org/10.1002/9783527641864.ch6>.
- [24] R.E. Dunin-Borkowski, T. Kasama, M.R. McCartney, D.J. Smith, *Electron holography*, *Sci. Microsc.* (2007) 1141–1195.
- [25] A. Tonomura, *Electron holography*, New ed., in: *Springer series in optical sciences*, vol. 70, Springer Berlin / Heidelberg, Berlin, Heidelberg, 2013.
- [26] E. Völkl, L.F. Allard, D.C. Joy, *Introduction to Electron Holography*, Springer New York, NY, 1999.
- [27] C. Zuo, J. Li, J. Sun, Y. Fan, J. Zhang, L. Lu, R. Zhang, B. Wang, L. Huang, Q. Chen, Transport of intensity equation: a tutorial, *Opt. Lasers Eng.* 135 (2020) 106187, <http://dx.doi.org/10.1016/j.optlaseng.2020.106187>.
- [28] M. Beleggia, M.A. Schofield, V.V. Volkov, Y. Zhu, On the transport of intensity technique for phase retrieval, *Ultramicroscopy* 102 (1) (2004) 37–49, <http://dx.doi.org/10.1016/j.ultramic.2004.08.004>.
- [29] M. Beleggia, T. Kasama, R.E. Dunin-Borkowski, The quantitative measurement of magnetic moments from phase images of nanoparticles and nanostructures—I. Fundamentals, *Ultramicroscopy* 110 (5) (2010) 425–432, <http://dx.doi.org/10.1016/j.ultramic.2009.10.007>.
- [30] R. Tomasello, E. Martinez, R. Zivieri, L. Torres, M. Carpentieri, G. Finocchio, A strategy for the design of skyrmion racetrack memories, *Sci. Rep.* 4 (1) (2014) 6784, <http://dx.doi.org/10.1038/srep06784>.
- [31] M. Chauwin, X. Hu, F. Garcia-Sanchez, N. Betrabet, A. Paler, C. Moutafis, J.S. Friedman, Skyrmion logic system for large-scale reversible computation, *Phys. Rev. Appl.* 12 (2019) 064053, <http://dx.doi.org/10.1103/PhysRevApplied.12.064053>.
- [32] S. Kaappa, S. Santa-aho, M. Honkanen, M. Vippola, L. Laurson, Magnetic domain walls interacting with dislocations in micromagnetic simulations, *Commun. Mater.* 5 (1) (2024) 256, <http://dx.doi.org/10.1038/s43246-024-00697-9>.
- [33] S. Kaappa, L. Laurson, Barkhausen noise from formation of 360° domain walls in disordered permalloy thin films, *Phys. Rev. Res.* 5 (2) (2023) L022006, <http://dx.doi.org/10.1103/PhysRevResearch.5.L022006>.
- [34] T. Herranen, L. Laurson, Barkhausen noise from precessional domain wall motion, *Phys. Rev. Lett.* 122 (2019) 117205, <http://dx.doi.org/10.1103/PhysRevLett.122.117205>.
- [35] A. Vansteenkiste, J. Leliaert, M. Dvornik, M. Helsen, F. Garcia-Sanchez, B.V. Waeyenberge, The design and verification of MuMax3, *AIP Adv.* 4 (2014) <http://dx.doi.org/10.1063/1.4899186>.
- [36] A. Hubert, R. Schäfer, *Magnetic Domains: the Analysis of Magnetic Microstructures*, Springer Science & Business Media, 2008.
- [37] Zenodo repository for our hologram processing code: 10.5281/zenodo.15279247, 2025, <http://dx.doi.org/10.5281/zenodo.15279247>.
- [38] M. Schofield, Y. Zhu, Fast phase unwrapping for interferometric applications, *Opt. Lett.* 28 (2003) 1194–1196, <http://dx.doi.org/10.1364/OL.28.001194>.
- [39] G. Bradski, *The OpenCV Library*, Dr. Dobb's J. Softw. Tools (2000).
- [40] J.M.D. Coey, *Magnetism and Magnetic Materials*, Cambridge University Press, 2010.
- [41] D. Chaira, B.K. Mishra, S. Sangal, Magnetic properties of cementite powder produced by reaction milling, *J. Alloys Compd.* 474 (1–2) (2009) 396–400, <http://dx.doi.org/10.1016/j.jallcom.2008.06.099>.
- [42] S. Yamamoto, T. Terai, T. Fukuda, K. Sato, T. Kakeshita, S. Horii, M. Ito, M. Yonemura, Magnetocrystalline anisotropy of cementite pseudo single crystal fabricated under a rotating magnetic field, *J. Magn. Magn. Mater.* 451 (2018) 1–4, <http://dx.doi.org/10.1016/j.jmmm.2017.10.114>.
- [43] W. Lottermoser, A.K. Schaper, W. Treutmann, G. Redhammer, G. Tippelt, A. Lichtenberger, S.-U. Weber, G. Amthauer, 57Fe Mössbauer spectroscopy on multiwalled carbon nanotubes with metal filling, *J. Phys. Chem. B* 110 (20) (2006) 9768–9771, <http://dx.doi.org/10.1021/jp061803x>.
- [44] D. Liu, J. Zhu, S. Ivaturi, Y. He, S. Wang, J. Wang, S. Zhang, M.A. Willis, F.S. Boi, Giant magnetic coercivity in Fe<sub>3</sub>C-filled carbon nanotubes, *RSC Adv.* 8 (25) (2018) 13820–13825, <http://dx.doi.org/10.1039/C7RA13671D>.
- [45] M. Beleggia, M.A. Schofield, Y. Zhu, M. Malac, Z. Liu, M. Freeman, Quantitative study of magnetic field distribution by electron holography and micromagnetic simulations, *Appl. Phys. Lett.* 83 (7) (2003) 1435–1437, <http://dx.doi.org/10.1063/1.1603355>.
- [46] J.A. Garlow, S.D. Pollard, M. Beleggia, T. Dutta, H. Yang, Y. Zhu, Quantification of mixed Bloch-Néel topological spin textures stabilized by the Dzyaloshinskii-Moriya interaction in Co/Pd multilayers, *Phys. Rev. Lett.* 122 (23) (2019) 237201, <http://dx.doi.org/10.1103/PhysRevLett.122.237201>.
- [47] Z. Schnepf, S.C. Wimbush, M. Antonietti, C. Giordano, Synthesis of highly magnetic iron carbide nanoparticles via a biopolymer route, *Chem. Mater.* 22 (18) (2010) 5340–5344, <http://dx.doi.org/10.1021/cm101746z>.
- [48] U. Atxitia, D. Hinzke, O. Chubykalo-Fesenko, U. Nowak, H. Kachkachi, O.N. Mryasov, R.F. Evans, R.W. Chantrell, Multiscale modeling of magnetic materials: Temperature dependence of the exchange stiffness, *Phys. Rev. B—Condensed Matter Mater. Phys.* 82 (13) (2010) 134440, <http://dx.doi.org/10.1103/PhysRevB.82.134440>.
- [49] T. Lатышевская, P. Formanek, C.T. Koch, A. Lubk, Off-axis and inline electron holography: Experimental comparison, *Ultramicroscopy* 110 (5) (2010) 472–482, <http://dx.doi.org/10.1016/j.ultramic.2009.12.007>.